RESEARCH ARTICLE
SOLID EARTH: GEOELECTROMAGNETICS

Earth and Planetary Physics
9: 677–685, 2025
doi: 10.26464/epp2025054

The global lithospheric field modeling based on MSS-1 and other satellites' gradient data

YuXuan Lin[1,2,3], Yan Feng[1,2,3*], JiaXuan Zhang[1,2,3,4], XinWu Li[1,2,3], and Ya Huang[2]

[1]Institute of Space Weather, School of Atmospheric Physics, Nanjing University of Information Science & Technology, Nanjing 210044, China;

[2]State Key Laboratory of Space Weather, Chinese Academy of Sciences, Beijing 100190, China;

[3]State Key Laboratory of Environment Characteristics and Effects for Near-space, Nanjing University of Information Science & Technology, Nanjing 210044, China;

[4]Macau Institute of Space Technology and Application, Macau University of Science and Technology, Macao 999078, China

Key Points:

- The 41° orbital inclination of the Macau Science Satellite-1 (MSS-1) provides near east–west gradient data.
- The modeling process incorporates data from the MSS-1, CHAMP (CHAllenging Minisatellite Payload), *Swarm-A*, and *Swarm-C* satellites.
- The models generated using east–west and north–south gradient data exhibit good agreement with existing models.

Citation: Lin, Y. X., Feng, Y., Zhang, J. X., Li, X. W., and Huang, Y. (2025). The global lithospheric field modeling based on MSS-1 and other satellites' gradient data. *Earth Planet. Phys.*, *9*(3), 677–685. http://doi.org/10.26464/epp2025054

Abstract: We combine gradient data from the Macau Science Satellite-1 (MSS-1), CHAllenging Minisatellite Payload (CHAMP), *Swarm-A*, and *Swarm-C* satellites to develop a 110-degree lithospheric magnetic field model. We then comprehensively evaluate the performance of the model by power spectral comparisons, correlation analyses, sensitivity matrix assessments, and comparisons with existing lithospheric field models. Results showed that using near east–west gradient data from MSS-1 significantly enhances the model correlation in the spherical harmonic degree (*N*) range of 45–60 while also mitigating the decline in correlation at higher degrees ($N > 60$). Furthermore, the unique orbital characteristics of MSS-1 enable its gradient data to provide substantial contributions to modeling in the mid- to low-latitude regions. With continued data acquisition from MSS-1 and further optimization of data processing methods, the performance of the model is expected to improve.

Keywords: lithospheric magnetic field; Macau Science Satellite-1; gradient data; LCS-1

1. Introduction

The lithospheric magnetic field arises from the induced and remanent magnetization of rocks, and its strength and distribution are largely influenced by factors such as mineralogy, temperature, chemical alteration, age, deformation, and the orientation of the Earth's main field (Dunlop and Özdemir, 2015). This magnetic field is crucial for geophysical exploration and geological structural interpretation.

High-quality modeling data are essential for developing lithospheric field models. Low earth orbit satellites are currently the most effective way to acquire global lithospheric magnetic field data. Early scalar measurements from the POGO (Polar Orbiting Geophysical Observatories) satellites resulted in the first global magnetic anomaly map (Regan et al., 1975). Subsequently, the Magsat satellites provided simultaneous vector and scalar data, enabling the creation of global vector and scalar magnetic anomaly maps (Arkani-Hamed et al., 1994). Data from the Ørsted satellite (Neubert et al., 2001), launched in February 1999, facilitated the development of early internal field spherical harmonic models (Olsen et al., 2000). The CHAMP (CHAllenging Minisatellite Payload) satellite (Reigber et al., 2002), launched in July 2000, delivered high-quality coverage that enabled the development of detailed lithospheric magnetic field models, including the MF (Magnetic Field Model) series (Maus et al., 2007, 2008), the CM (Comprehensive Model) series (Sabaka et al., 2004, 2015), and the CHAOS (the CHAMP, Ørsted and SAC-C model) series (Olsen et al., 2006, 2009, 2010, 2014). The *Swarm* satellites (Friis-Christensen et al. 2006) were launched in November 2013. The *Swarm* satellite constellation consists of three near polar-orbit satellites, with *Swarm-A* and *Swarm-C* flying side by side. The orbital altitude is approximately 465 km, with a local time difference of 6 minutes between them. Their longitude difference is approximately 1.4°, and the east–west distance is 155 km.

Satellites cannot directly observe gradient data, so such data are typically derived from along-track magnetic field differences. Since Kotsiaros et al. (2015) first demonstrated the advantages of

First author: Y. X. Lin, eins_lin@163.com
Correspondence to: Y. Feng, frank_feng8848@163.com
Received 20 DEC 2024; Accepted 31 MAR 2025.
First Published online 21 APR 2025.

along-track magnetic field differences, such measurements have become an essential component of magnetic field modeling. The *Swarm* satellite constellation enabled multi-satellite observations, thereby extending gradient data applications beyond the north–south direction, as shown in the studies by Olsen et al. (2016) and Kotsiaros (2016). Moreover, Olsen et al. (2015) demonstrated that using spatial differences in scalar data significantly improved the quality of lithospheric field and long-term variation models in the SIFM (*Swarm* Initial Field Model). Consistent with these findings, spatial gradients in scalar data have been shown to enhance model accuracy in the CHAOS-6 (the CHAMP, Ørsted and SAC-C model-6; Finlay et al., 2016), DLFI (Dedicated Lithospheric Field Inversion; Thébault et al., 2016), and LCS-1 (Lithospheric model derived from CHAMP and Swarm satellite data-1; Olsen et al., 2017) models. The LCS-1 model improves spatial resolution and suppresses noise through the integration of high-quality datasets from the *Swarm* and CHAMP missions. It utilizes L1-norm regularization. Compared with traditional L2-norm regularization, the L1-norm better preserves localized high-amplitude features while suppressing spurious signals in low-amplitude regions. Overall, the LCS-1 model substantially improves model accuracy.

The Macau Science Satellite-1 (MSS-1), which focuses on geomagnetic field research at the middle- and low-latitude areas with unprecedented high-precision data (Zhang K, 2023) , was launched in May 2023. Its orbital inclination is 41°, and by performing along-track differencing on its observational data, we can obtain preliminary gradient data in both the northeast–southwest and northwest–southeast directions. These near east–west gradient data may largely make a substantial contribution to lithospheric magnetic field modeling, especially by improving model accuracy in the mid- to low-latitude regions.

Division of the different sources of the geomagnetic field is a difficult issue in modeling, especially for low-intensity fields such as the tidal magnetic field. Grayver and Olsen (2019) reported that tidal field perturbations at satellite altitudes can reach up to 3–4 nT. However, few existing models remove tidal fields from the modeling data. In this study, we address this limitation by applying models to eliminate tidal fields, thereby maximizing data quality. Moreover, we combine gradient data from the CHAMP, *Swarm*, and MSS-1 to construct a lithospheric magnetic field model up to spherical harmonic degree 110, with particular focus on the role of MSS-1 gradient data. Section 2 details the criteria for satellite data selection and processing, whereas Section 3 describes the modeling methodology. Section 4 presents the results, including comparisons with existing models and an analysis of the contributions of MSS-1 data. Finally, Section 5 summarizes the findings and discusses the potential of MSS constellation data for advancing future geomagnetic research.

2. Data Selection

To construct the lithospheric magnetic field model, we used data from three satellite missions. We selected CHAMP data from January 2008 to September 2010, when solar activity was low (to reduce ionospheric and magnetospheric influences) and the altitude was relatively low. Meanwhile, *Swarm* data collected from March 2022 to October 2024 provided the most recent dataset available at the time of selection. These data were aligned as closely as possible in time with the MSS-1 data to minimize errors caused by temporal variations. Additionally, we selected one full year of MSS-1 observations, from November 2023 to October 2024, for modeling.

For consistency, we adopted the data selection criteria used in the CHAOS model series (Finlay et al., 2020) by regarding them as geomagnetically quiet periods. The specific selection criteria are as follows:

(1) Data with a solar zenith angle at least 10° below the horizon were selected, to minimize ionospheric current contributions;

(2) The variation in the ring current (RC) index across all latitudes was restricted to $\leq$2 nT/h;

(3) The geomagnetic activity index (*Kp*) was required to be $\leq$2°;

(4) The 1-minute average of the magnetospheric merging electric field (E_m), calculated over the preceding 2 hours, was limited to $\leq$0.8 mV/m;

(5) The 2-hour averaged interplanetary magnetic field (IMF) $B_z > 0$;

(6) For quasi-dipole (QD) latitudes > 0 (Richmond et al., 1995), the 2-hour averaged IMF $B_y < 3$ nT; for QD latitudes < 0, IMF $B_y > -3$ nT;

(7) Within the equatorial QD latitude ±55° region, both vector and scalar data were utilized;

(8) Beyond the equatorial QD latitude ±55° region, only scalar data were used.

The data selection criteria were fully applied to the CHAMP and *Swarm* datasets. However, because of the relatively limited number of MSS-1 data since launch, we adopted slightly relaxed selection criteria to broaden its observational coverage and maximize its contribution to the modeling. The MSS-1 data selection excluded the E_m and IMF conditions.

Before modeling, we removed the core field B_{core} and the external fields B_{ext} from observational data B_{obs} by using the first 15 spherical harmonic degrees and the external part of the CHAOS-7.18 model (Finlay et al. 2020). We also utilized the tidal field model by Grayver and Olsen (2019) to remove tidal field B_{tid} contributions from the observational data:

$$B_{lith} = B_{obs} - B_{core} - B_{ext} - B_{tid} - \varepsilon. \quad (1)$$

Here, B_{lith} represents the lithospheric field signal required for modeling, whereas ε denotes the residual error, primarily originating from unmodeled fields.

The north–south gradient approximated by the differences $\Delta B_{NS} = B(t_2) - B(t_1), (t_2 > t_1)$ was calculated from CHAMP and *Swarm-A* observations, whereas the east–west gradient approximated by the differences $\Delta B_{Swarm-EW} = B(A) - B(C)$ was derived from *Swarm-A* and *Swarm-C* observations, respectively, within a 50-second temporal difference at the same latitude. Because the MSS-1 has an orbital inclination of only 41°, the along-track differences $\Delta B_{MSS-EW} = B(t_2) - B(t_1), (t_2 > t_1)$ were the approximations of east–west gradients.

Finally, because external magnetic fields are generally large-scale phenomena and tend to cancel out when differencing adjacent measurements, we assigned a relatively small prior error to the gradient data (Olsen et al., 2015). Figure 1 presents the total volume of gradient data selected and calculated for modeling, along with their latitudinal distribution. Because the MSS-1 vector data were less than 10,000 after the final selection, we did not

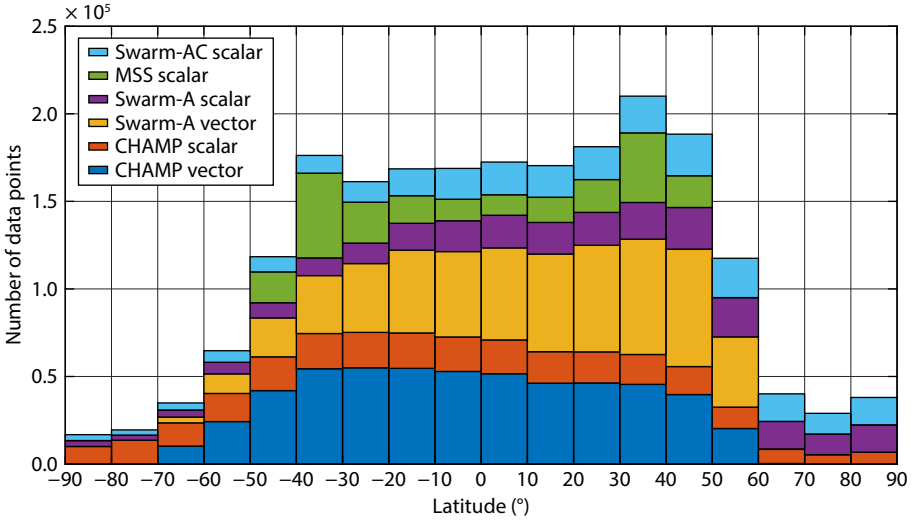

Figure 1. Variation in data numbers with latitude.

combine them into the modeling process. To address data gaps in the high-latitude polar regions (87.3°–89.9°), we supplemented these areas with 3600 model-generated data points from the CHAOS-7.18 model.

3. Modeling Methods

The lithospheric field of the internal source field is generally assumed to be unchanging. Furthermore, the data sampling region is considered free of current influences (Kotsiaros et al., 2015). Under these assumptions, a potential field model is utilized, allowing the vector magnetic field $\boldsymbol{B}$ at any location within the region to be expressed as the gradient of a scalar magnetic potential V:

$$\boldsymbol{B} = \begin{bmatrix} -B_\theta \\ +B_\phi \\ -B_r \end{bmatrix} = -\nabla V. \tag{2}$$

The potential V satisfies Laplace's equation and can be expanded in the geocentric Earth-fixed coordinate system as follows:

$$V(r,\theta,\phi) = a\sum_{n=1}^{N_{\rm int}}\sum_{m=0}^{n}\left(\frac{a}{r}\right)^{n+1}\left[g_n^m\cos(m\phi)+h_n^m\sin(m\phi)\right]P_n^m(\cos\theta). \tag{3}$$

Here, a = 6371.2 km is chosen as the reference radius of Earth's surface; (r,θ,ϕ) represents the geographic coordinates, where r is the geocentric distance, θ is the colatitude, and ϕ is the geographic longitude; and P_n^m denotes the associated Schmidt seminormalized Legendre functions (Winch et al. 2005). Set $\{g_n^m, h_n^m\}$ corresponds to the Gauss coefficients describing the internal source field, and $N_{\rm int}$ represents the maximum degree and order of the expansion. In this study, the lithospheric field is truncated at $N_{\rm int}$ = 110, resulting in a total of 110 × 112 = 12,320 coefficients used to describe the lithospheric field.

Thus, the determination of spherical harmonic coefficients can be formulated as a linear system:

$$\boldsymbol{Gm} = \boldsymbol{d}, \tag{4}$$

where $\boldsymbol{G}$ represents the kernel matrix containing the basis function, $\boldsymbol{m}$ denotes the vector of modified spherical harmonic coefficients, and $\boldsymbol{d}$ is the vector of observational data. To estimate the model coefficients $\boldsymbol{m} = \{g_n^m, h_n^m\}$ from satellite magnetic field data, we apply the least-squares method. All observational data $\boldsymbol{B}_{\rm obs}$ are consolidated into a single vector $\boldsymbol{d}_{\rm obs}$, and similarly, the model-computed data at the same locations $\boldsymbol{B}_m$ are consolidated into a single vector $\boldsymbol{d}_m$. The residual vector $\boldsymbol{e} = \boldsymbol{d}_{\rm obs} - \boldsymbol{d}_m$ is minimized to achieve the best fit.

However, because of the incompleteness of our model (unmodeled fields exist), the residual $\boldsymbol{e}$ does not follow a Gaussian distribution. Under such conditions, the standard least-squares method cannot reliably estimate the model parameters (Walker and Jackson, 2000). To address this issue, we used an iterative reweighted least-squares (IRLS) method (Constable, 1988), which provides a more robust fit to the satellite data:

$$\boldsymbol{m} = (\boldsymbol{G}^{\rm T}\boldsymbol{W}_d^{\rm T}\boldsymbol{W}_d\boldsymbol{G})^{-1}\boldsymbol{G}^{\rm T}\boldsymbol{W}_d^{\rm T}\boldsymbol{W}_d\boldsymbol{d}, \tag{5}$$

where the superscript T denotes the transpose of the matrix, and $\boldsymbol{W}_d$ denotes the initial data weighting matrix:

$$\boldsymbol{W}_d = {\rm diag}\left(\frac{\sin\theta}{\sigma_i}\right), \tag{6}$$

where σ_i represents the standard deviation of the ith observation, and θ denotes the colatitude of the observation point in the spherical coordinate system. If the data are sampled based on a regular grid in longitude and latitude, the data distribution will be denser in high-latitude regions. To prevent overfitting in these densely sampled areas during the inversion process, a weight proportional to $\sin\theta$ is applied to each data point.

4. Results and Discussion

To evaluate the potential contribution of the newly acquired MSS-1 data to lithospheric magnetic field modeling, in this study we designed a series of analyses aimed at comparing the effects of different gradient datasets on model accuracy. In Table 1, we list the modeling of gradient data and related results.

Table 1 provides the total number of data points from each satellite, along with residual fitting errors between observed values

Table 1. The vector (*X*, *Y*, *Z*) and scalar (*F*) gradient data points used for modeling from different satellites, along with their mean fitting error (in nanoteslas) and root mean square error (RMS, in nanoteslas).

Variable	CHAMP			*Swarm-A*			MSS-1			*Swarm-A – Swarm-C*		
	N	Mean	RMS	*N*	Mean	RMS	*N*	Mean	RMS	*N*	Mean	RMS
X (NS)	543,179	0	0.30	547,666	−0.04	0.28						
Y (NS)	543,179	0	0.35	547,666	−0.01	0.32						
Z (NS)	543,179	0	0.29	547,666	−0.09	0.31						
F (NS)	272,959	−0.01	0.25	246,190	−0.02	0.33						
F (EW)							220,097	0	0.55	223,955	−0.07	0.47

and final model predictions. These errors are quantified by their mean and root mean square (RMS) values of unweighted results, computed from the model residuals $\boldsymbol{e} = \boldsymbol{d}_{\rm obs} - \boldsymbol{d}_m$. Among all the scenarios, the combination of vector and scalar gradient data demonstrated the best-fitting performance.

North–south gradient data, primarily from the CHAMP and *Swarm-A* satellites, achieved the lowest RMS fitting errors (approximately 0.25–0.35 nT). In contrast, using only scalar gradient data yielded relatively larger fitting errors for east–west gradients, 0.55 nT for MSS-1 and 0.47 nT for *Swarm-A* and *Swarm-C*.

It should be noted that because of the limited number of MSS-1 data, the selection criteria were suitably relaxed during processing and filtering to maximize the inclusion of MSS-1 measurements. Within this framework, the results aligned with expectations, confirming both scientific validity and reasonable accuracy. Consequently, MSS-1 data could be effectively combined with other satellite datasets, offering a valuable addition to lithospheric magnetic field modeling data.

We conducted a series of analyses by using different gradient datasets. Specifically, we compared two scenarios: (1) modeling based solely on gradient data from the CHAMP, *Swarm-A*, and *Swarm-C* satellites; and (2) modeling that additionally incorporated MSS-1 gradient data. The model including MSS-1 data is referred to as the MSS-1, *Swarm*, CHAMP Magnetic Gradient Model (MSCMGM), whereas the model without MSS-1 data is named the *Swarm*, CHAMP Magnetic Gradient Model (SCMGM).

We examined the modeling results from three perspectives: (1) by comparing power spectra with existing models, (2) by evaluating correlations with prior spherical harmonic coefficients and corresponding sensitivity matrices, and (3) by comparing global radial component distribution maps obtained by forward modeling of the final coefficients.

To assess the reliability of our final model, we first conducted a comparative analysis of its power spectrum with those of other models. The detailed results are shown in Figure 2. Figure 2 compares the power spectrum of the MSCMGM, constructed using gradient data from four satellites, with those of previous models (LCS-1, MF7 (Maus, 2010), and CM6 (Sabaka et al., 2020)), and it shows the differences among these power spectra. For

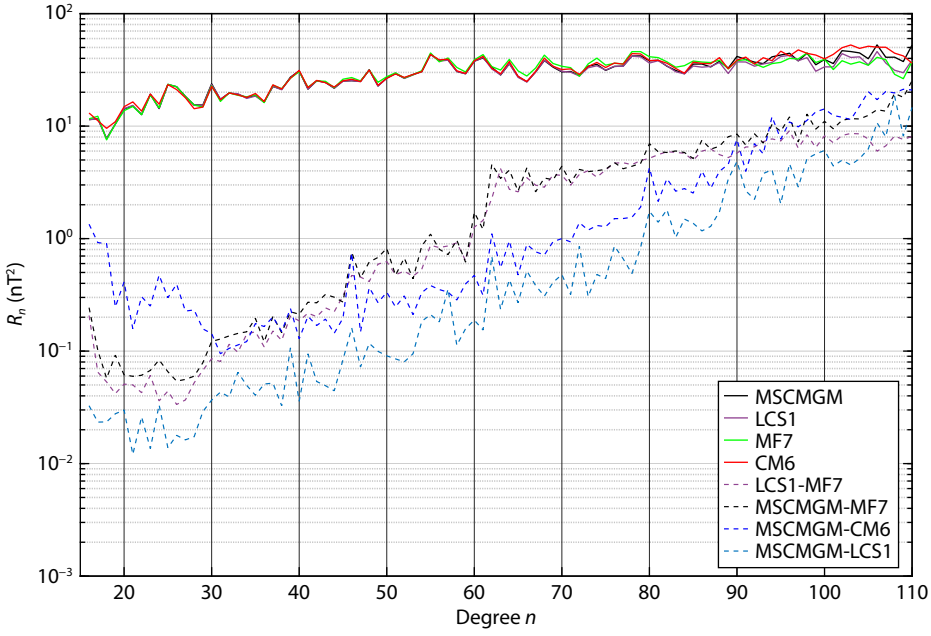

Figure 2. Comparison of the Mauersberger–Lowes power spectrum (in nT^2) for lithospheric field models MSCMGM (black), LCS1 (purple), MF7 (green), and CM6 (red), along with their difference spectra: LCS1–MF7 (purple dashed), MSCMGM–MF7 (black dashed), MSCMGM–CM6 (dark blue dashed), and MSCMGM–LCS1 (light blue dashed).

spherical harmonic degrees $N \leq 70$, the power spectrum of the MSCMGM aligns well with other models, indicating a high degree of consistency. However, as N increases beyond 70, deviations from the prior models become increasingly apparent, particularly in the range of $N = 90$ to $N = 110$.

These deviations may arise from various steps in the data processing phase. Additionally, interference from unmodeled geomagnetic signals, such as those originating from the ionosphere, the magnetosphere, or small-scale geomagnetic anomalies, may further contribute to the observed discrepancies.

Overall, these findings suggest that although the new model performs reliably when the degree is less than 70, further refinements in data processing methods or the incorporation of additional prior information may be necessary to improve high-degree modeling and mitigate the impact of external unmodeled fields on the results.

In addition to comparing the power spectra, common methods for assessing model reliability include calculating correlation coefficients and sensitivity matrices. These methods were also applied in this study, where we compared the scenarios with and without MSS-1 data, as shown in Figures 3a and 3b.

Figure 3a illustrates the variation in correlation coefficients between the MSCMGM and three prior models (LCS-1, MF7, and CM6). For $N \leq 60$, these coefficients remain high, even close to 1, across all comparisons. As the spherical harmonic degree increases beyond 61, the correlation coefficients gradually decrease but still remain above 0.9 until $N = 90$. Between $N = 90$ and $N = 110$, the coefficients with the CM6 model show a more pronounced decline, consistent with the power spectrum results. When $N > 110$, the correlation coefficients for each model decrease rapidly. Consequently, we regard the subsequent coefficients as unreliable and establish the maximum order at 110.

Overall, the correlation coefficients with LCS-1 remain the highest, which aligns with the choice of using LCS-1 as the prior model during data processing. Even at $N = 110$, correlations with LCS-1, MF7, and CM6 exceed 0.73, indicating that, despite variations in satellite data sources and modeling methods, the lithospheric magnetic field solutions from different models are largely consistent. Furthermore, the four-satellite model demonstrates robust reliability.

Figure 3b shows the correlation coefficients between the SCMGM (based solely on CHAMP, *Swarm-A*, and *Swarm-C* data) and the same set of prior models. In comparison with the correlation coefficients in Figure 3a, incorporating MSS-1 gradient data raises the correlation coefficients in the $N = 45$–60 range and alleviates the downward trend beyond $N = 60$. By $N = 110$, the correlation coefficients in the four-satellite scenario surpass those of the three-satellite scenario, with the minimum coefficient increasing from 0.70 to 0.73. This result underscores the positive impact of MSS-1 data on improving model accuracy.

Additionally, Figures 3c and 3d present sensitivity matrices of

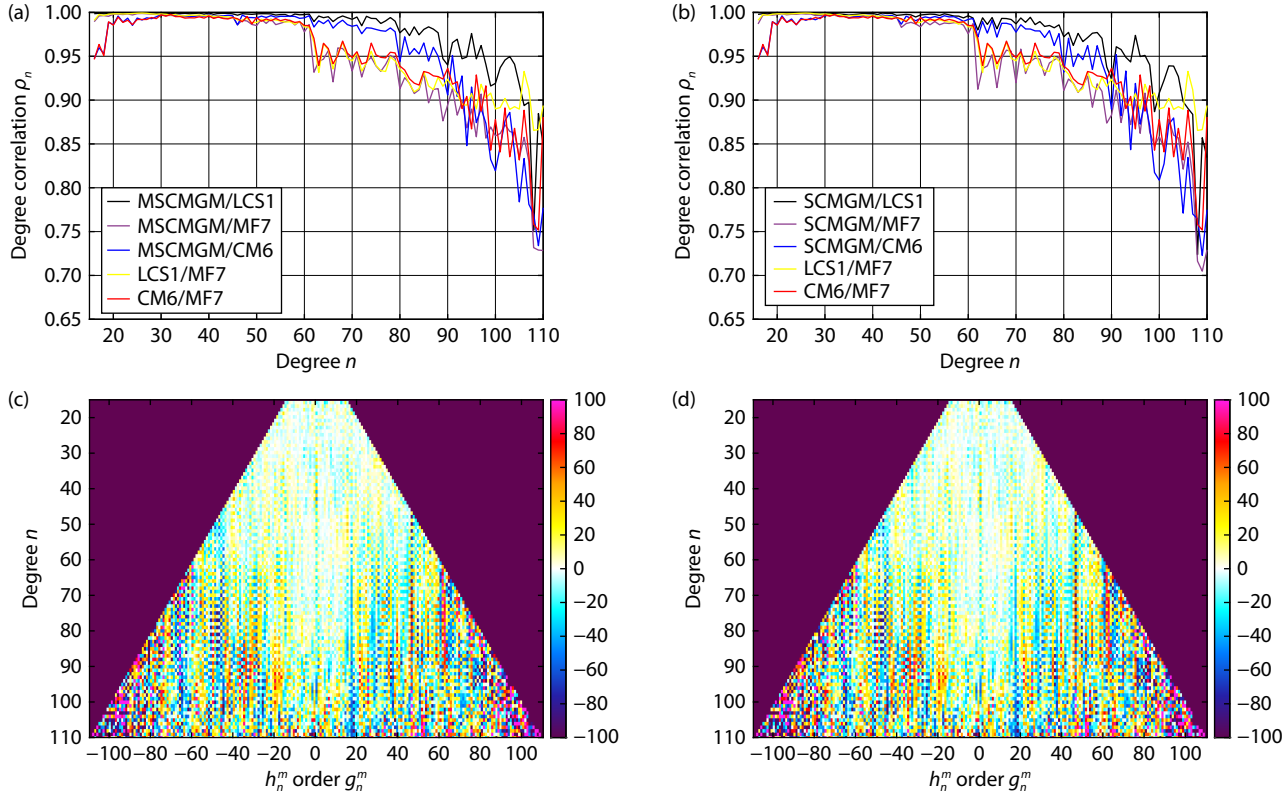

Figure 3. Correlation of models constructed from different gradient datasets with established models (LCS-1, MF7, CM6), and sensitivity matrices (normalized coefficient differences in percent) of Gauss coefficients on degree n and order m. (a) Correlation coefficients of the MSCMGM compared with LCS-1, MF7, and CM6; (b) correlation coefficients of the SCMGM compared with LCS-1, MF7, and CM6; (c) sensitivity matrix of the MSCMGM against MF7; (d) sensitivity matrix of the SCMGM against MF7.

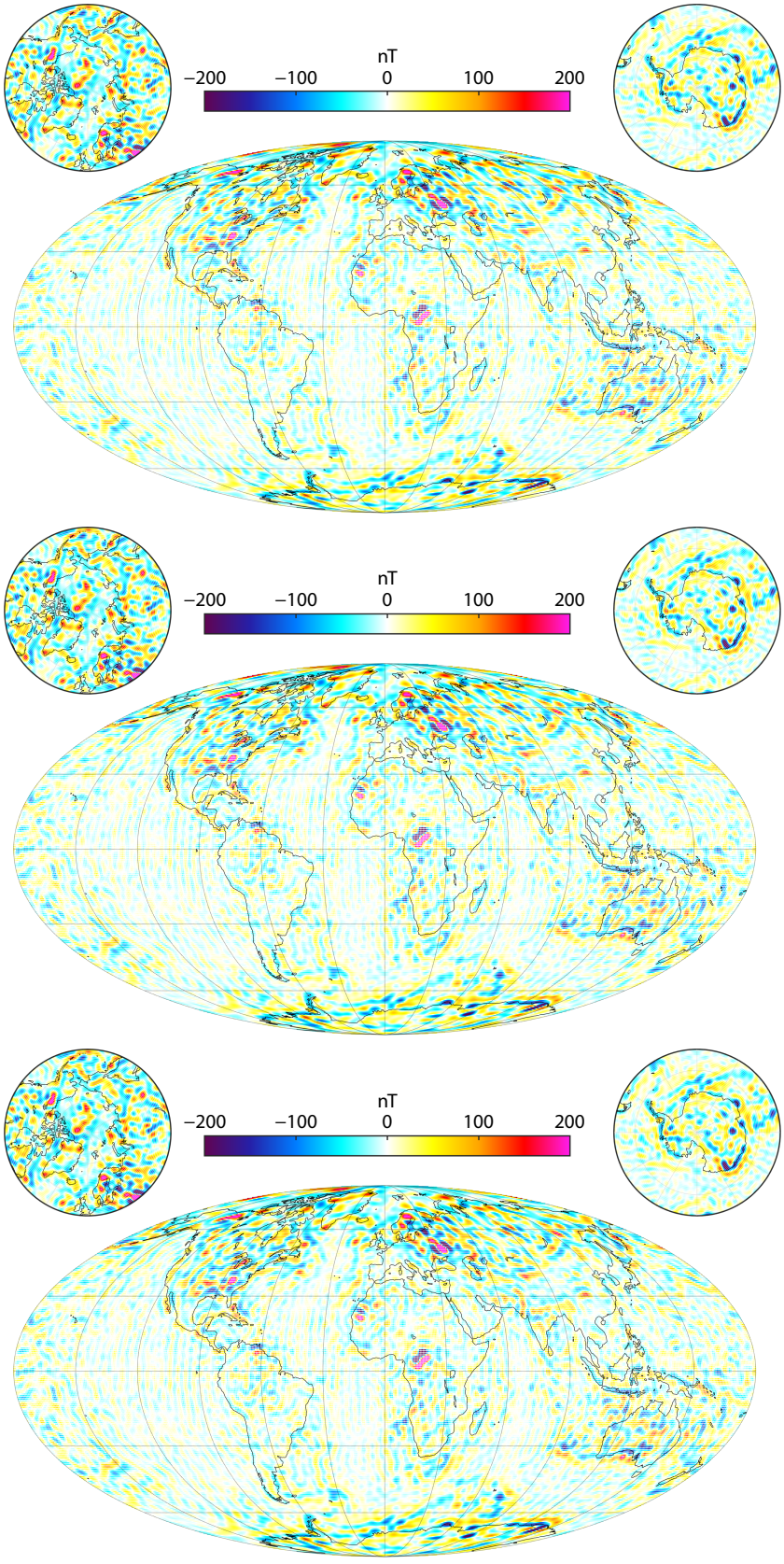

Figure 4. Global distribution maps of the radial component at the surface. (top) Global distribution of the MSCMGM; (middle) global distribution of the SCMGM; (bottom) global distribution of the LCS-1.

models constructed from different datasets with respect to the MF7 model. Comparisons of these matrices revealed no substantial discrepancies, which can be attributed to the currently limited volume of MSS-1 observations. As MSS-1 data continue to accumulate, we anticipate further enhancements in model accuracy and the identification of additional geomagnetic features.

Finally, we analyzed the contribution of MSS-1 gradient data to the modeling by comparing the forward modeling results. Because of the high consistency between the coefficients, we refrained from comparing the differences with other models and instead focused solely on the differences between the scenarios with and without MSS-1 data. The forward modeling results for the global surface radial component are presented in Figure 4.

Figure 4 presents the forward modeling results of the radial component at the Earth's surface for different models. The top panel shows the global surface radial component obtained by the MSCMGM, offering a detailed depiction of lithospheric magnetic field features. The distribution is highly consistent with those of other global models.

The middle panel displays the global surface radial component when using only the gradient data from the SCMGM. The bottom panel displays the global surface radial component from the LCS-1 model, which is also a model derived from gradient data from CHAMP and *Swarm*. By comparing these three images, we can observe that their overall trends and structures remain highly consistent, with no discernible large-scale differences in prominent magnetic anomalies.

To investigate the specific differences, we subtracted the forward results and present the differences between these models in Figure 5. Figure 5 shows that significant differences in both comparisons are mainly found in the mid- to low-latitude regions, consistent with the orbital coverage of the MMS-1 mission. We believe this result intuitively reflects the contribution of MMS-1 data to the modeling process. These differences may arise from unmodeled disturbances in external magnetic fields, such as the

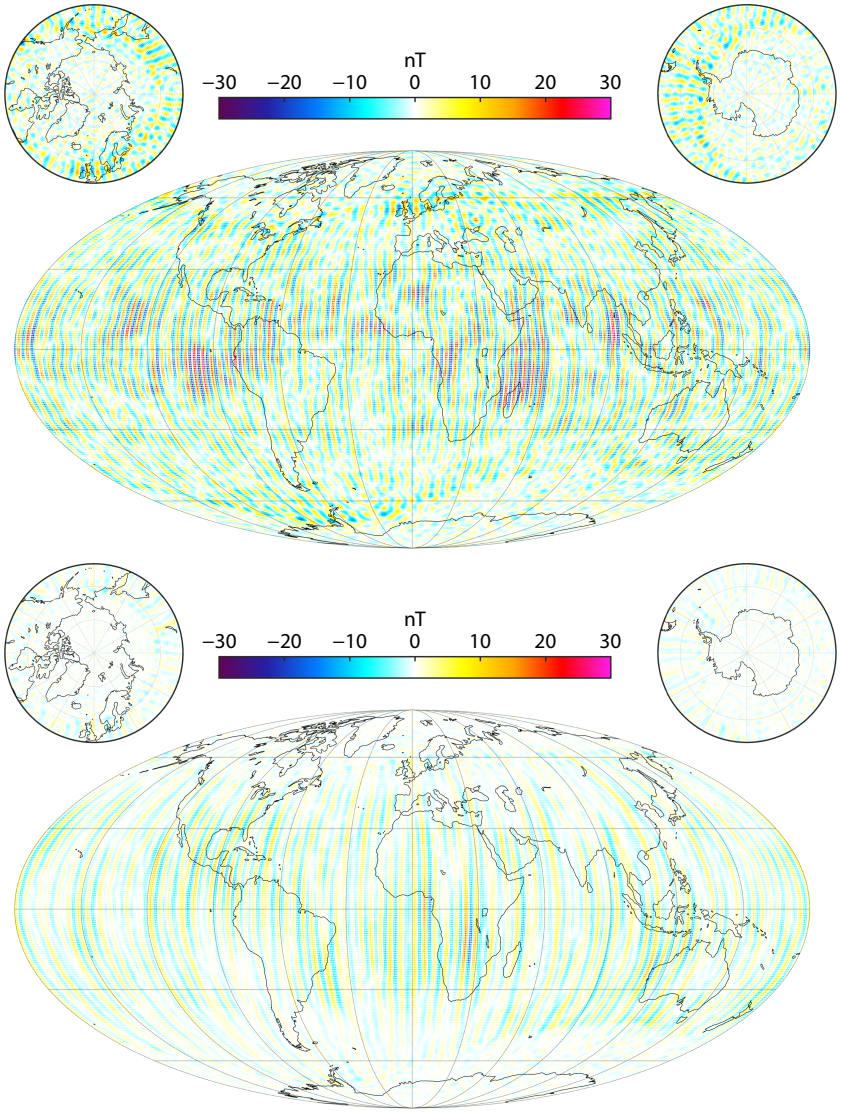

Figure 5. Difference map between the two forward results. (top) Differences between the MSCMGM and LCS-1; (bottom) differences between the MSCMGM and SCMGM.

effects of equatorial electrojets. Although using along-track differences and gradient data helps address this issue, it cannot completely eliminate the effects of rapid variations and small-scale disturbances. Because of the unique orbit of the MMS-1, it can observe more features in the equatorial region.

The differences exhibit a north–south striping pattern, which does not align with the expected southeast–northwest or northeast–southwest striping along the MMS-1 trajectory. We attribute this result to the dominance of north–south gradient data in the dataset. It is significant that the most pronounced differences between the MSCMGM and SCMGM are found on either side of the Bangui magnetic anomaly in Africa. We cannot currently determine whether these differences are due to the MMS-1 capturing more magnetic anomaly information or other influences. Further validation with additional datasets is necessary to clarify this observation.

Overall, the observed discrepancies largely stem from various unmodeled fields, such as those produced by ionospheric and magnetospheric current systems. This outcome points to areas requiring improvement in current data processing and selection, particularly the need to further suppress nonlithospheric magnetic signals in high-precision modeling. In future work, we plan to adopt more advanced filtering and decomposition techniques to minimize the effects of unmodeled fields, thereby boosting the reliability and accuracy of our model.

5. Conclusions and Outlook

In this study, we assessed the potential contribution of MSS-1 gradient data to lithospheric magnetic field modeling by integrating it with data from CHAMP, *Swarm-A*, and *Swarm-C*. Through correlation coefficient analyses, sensitivity matrices, power spectrum comparisons, and forward radial component distributions, we found that MSS-1 data substantially improves model accuracy, especially in the spherical harmonic degree range of $N = 45$ to 60. Furthermore, these data enhance correlation coefficients and mitigate their decline at higher degrees ($N > 60$). This is because gradient data can enhance the recovery of small-scale features in lithospheric magnetic field models and substantially reduce the need for corrections of external field contributions.

Power spectrum comparisons indicate a strong agreement with established models (e.g., LCS-1, MF7, CM6) for $N \leq 70$. However, discrepancies emerge when $N > 90$, likely attributable to unmodeled fields. Forward difference analyses also reveal certain limitations in the MSS-1 dataset, which is affected by external fields and constrained by its limited volume. Nonetheless, MSS-1 data make a substantial contribution to mid- to low-latitude modeling, underscoring their value in bolstering overall model reliability.

Future efforts should focus on expanding MSS-1 data collection to enlarge the database, whereas advanced techniques, such as temporal filtering and singular spectrum analysis, could further suppress external field interference. Additionally, combining data from satellites with complementary orbits may enhance both model resolution and reliability. By pursuing these strategies, researchers can more effectively exploit MSS-1 gradient data for high-precision lithospheric magnetic field studies. We also expect the upcoming MSS satellite, MSS-2, to be able to provide more high-quality gradient data to make a better model.

Acknowledgments

We acknowledge the support of the National Natural Science Foundation of China (Nos. 42250103, 41974073, and 41404053), the Macau Foundation and the preresearch project of Civil Aerospace Technologies (Nos. D020308 and D020303), which was funded by China's National Space Administration, the Specialized Research Fund for State Key Laboratories.

Open Research

The *Swarm* data are available at https://swarm-diss.eo.esa.int/#swarm%2FLevel1b%2FEntire_mission_data%2FMAGx_LR, the CHAMP satellite data can be downloaded from ftp://anonymous@isdcftp.gfz-potsdam.de/champ/, the MSS-1 data are available at https://mss.must.edu.mo/data.html, CHAOS-7 is available at http://www.spacecenter.dk/files/magnetic-models/CHAOS-7/, LCS-1 is available at http://www.spacecenter.dk/files/magnetic-models/LCS-1/, MF7 is available at https://geomag.colorado.edu/magnetic-field-model-mf7.html, and CM6 is available at http://www.spacecenter.dk/files/magnetic-models/CM6/.

References

Arkani-Hamed, J., Langel, R. A., and Purucker, M. (1994). Scalar magnetic anomaly maps of Earth derived from POGO and Magsat data. *J. Geophys. Res.: Solid Earth*, *99*(B12), 24075–24090. https://doi.org/10.1029/94jb00930

Constable, C. G. (1988). Parameter estimation in non-Gaussian noise. *Geophys. J. Int.*, *94*(1), 131–142. https://doi.org/10.1111/j.1365-246x.1988.tb03433.x

Dunlop, D. J., and Özdemir, Ö. (2015). Magnetizations in rocks and minerals. In G. Schubert (Ed.), *Treatise on Geophysics* (2nd ed, Vol. 5, pp. 255-308). Amsterdam: Elsevier. https://doi.org/10.1016/b978-0-444-53802-4.00102-0

Finlay, C. C., Olsen, N., Kotsiaros, S., Gillet, N., and Tøffner-Clausen, L. (2016). Recent geomagnetic secular variation from Swarm and ground observatories as estimated in the CHAOS-6 geomagnetic field model. *Earth Planets Space*, *68*(1), 112. https://doi.org/10.1186/s40623-016-0486-1

Finlay, C. C., Kloss, C., Olsen, N., Hammer, M. D., Tøffner-Clausen, L., Grayver, A., and Kuvshinov, A. (2020). The CHAOS-7 geomagnetic field model and observed changes in the South Atlantic Anomaly. *Earth Planets Space*, *72*(1), 156. https://doi.org/10.1186/s40623-020-01252-9

Friis-Christensen, E., Lühr, H., and Hulot, G. (2006). *Swarm*: A constellation to study the Earth's magnetic field. *Earth Planets Space*, *58*(4), 351–358. https://doi.org/10.1186/bf03351933

Grayver, A. V., and Olsen, N. (2019). The magnetic signatures of the M_2, N_2, and O_1 oceanic tides observed in Swarm and CHAMP satellite magnetic data. *Geophys. Res. Lett.*, *46*(8), 4230–4238. https://doi.org/10.1029/2019GL082400

Kotsiaros, S., Finlay, C. C., and Olsen, N. (2015). Use of along-track magnetic field differences in lithospheric field modelling. *Geophys. J. Int.*, *200*(2), 880–889. https://doi.org/10.1093/gji/ggu431

Kotsiaros, S. (2016). Toward more complete magnetic gradiometry with the Swarm mission. *Earth Planets Space*, *68*(1), 130. https://doi.org/10.1186/s40623-016-0498-x

Maus, S., Lühr, H., Rother, M., Hemant, K., Balasis, G., Ritter, P., and Stolle, C. (2007). Fifth-generation lithospheric magnetic field model from CHAMP satellite measurements. *Geochem. Geophys. Geosyst.*, *8*(5), Q05013. https://doi.org/10.1029/2006gc001521

Maus, S., Yin, F., Lühr, H., Manoj, C., Rother, M., Rauberg, J., Michaelis, I., Stolle, C., and Müller, R. D. (2008). Resolution of direction of oceanic magnetic lineations by the sixth-generation lithospheric magnetic field model from CHAMP satellite magnetic measurements. *Geochem. Geophys. Geosyst.*, *9*(7),

Q07021. https://doi.org/10.1029/2008gc001949

Maus, S. (2010). Magnetic field model MF7. https://www.geomag.us/models/MF7.html

Neubert, T., Mandea, M., Hulot, G., von Frese, R., Primdahl, F., Jørgensen, J. L., Friis-Christensen, E., Stauning, P., Olsen, N., and Risbo, T. (2001). Ørsted satellite captures high-precision geomagnetic field data. *Eos, Trans. AGU*, *82*(7), 81-88. https://doi.org/10.1029/01eo00043

Olsen, N., Holme, R., Hulot, G., Sabaka, T., Neubert, T., Tøffner-Clausen, L., Primdahl, F., Jørgensen, J., Léger, J. M., … Voorhies, C. (2000). Ørsted Initial Field Model. *Geophys. Res. Lett.*, *27*(22), 3607–3610. https://doi.org/10.1029/2000gl011930

Olsen, N., Lühr, H., Sabaka, T. J., Mandea, M., Rother, M., Tøffner-Clausen, L., and Choi, S. (2006). CHAOS-a model of the Earth's magnetic field derived from CHAMP, Ørsted, and SAC-C magnetic satellite data. *Geophys. J. Int.*, *166*(1), 67–75. https://doi.org/10.1111/j.1365-246x.2006.02959.x

Olsen, N., Mandea, M., Sabaka, T. J., and Tøffner-Clausen, L. (2009). CHAOS-2—a geo-magnetic field model derived from one decade of continuous satellite data. *Geophys. J. Int.*, *179*(3), 1477–1487. https://doi.org/10.1111/j.1365-246x.2009.04386.x

Olsen, N., Mandea, M., Sabaka, T. J., and Tøffner-Clausen, L. (2010). The CHAOS-3 geomagnetic field model and candidates for the 11th generation IGRF. *Earth Planets Space*, *62*(10), 719–727. https://doi.org/10.5047/eps.2010.07.003

Olsen, N., Lühr, H., Finlay, C. C., Sabaka, T. J., Michaelis, I., Rauberg, J., and Tøffner-Clausen, L. (2014). The CHAOS-4 geomagnetic field model. *Geophys. J. Int.*, *197*(2), 815–827. https://doi.org/10.1093/gji/ggu033

Olsen, N., Hulot, G., Lesur, V., Finlay, C. C., Beggan, C., Chulliat, A., Sabaka, T. J., Floberghagen, R., Friis-Christensen, E., … Vigneron, P. (2015). The Swarm Initial Field Model for the 2014 geomagnetic field. *Geophys. Res. Lett.*, *42*(4), 1092–1098. https://doi.org/10.1002/2014gl062659

Olsen, N., Finlay, C. C., Kotsiaros, S., and Tøffner-Clausen, L. (2016). A model of Earth's magnetic field derived from 2 years of Swarm satellite constellation data. *Earth Planets Space*, *68*(1), 124. https://doi.org/10.1186/s40623-016-0488-z

Olsen, N., Ravat, D., Finlay, C. C., and Kother, L. K. (2017). LCS-1: a high-resolution global model of the lithospheric magnetic field derived from CHAMP and Swarm satellite observations. *Geophys. J. Int.*, *211*(3), 1461–1477. https://doi.org/10.1093/gji/ggx381

Regan, R. D., Cain, J. C., and Davis, W. M. (1975). A global magnetic anomaly map. *J. Geophys. Res.*, *80*(5), 794–802. https://doi.org/10.1029/JB080i005p00794

Reigber, C., Luhr, H., and Schwintzer, P. (2002). Champ mission status. *Adv. Space Res.*, *30*(2), 129–134. https://doi.org/10.1016/S0273-1177(02)00276-4

Richmond, A. D. (1995). Ionospheric electrodynamics using Magnetic Apex Coordinates. *J. Geomagn. Geoelectr.*, *47*(2), 191–212. https://doi.org/10.5636/jgg.47.191

Sabaka, T. J., Olsen, N., and Purucker, M. E. (2004). Extending comprehensive models of the Earth's magnetic field with Ørsted and CHAMP data. *Geophys. J. Int.*, *159*(2), 521–547. https://doi.org/10.1111/j.1365-246x.2004.02421.x

Sabaka, T. J., Olsen, N., Tyler, R. H., and Kuvshinov, A. (2015). CM5, a pre-Swarm comprehensive geomagnetic field model derived from over 12 yr of CHAMP, Ørsted, SAC-C and observatory data. *Geophys. J. Int.*, *200*(3), 1596–1626. https://doi.org/10.1093/gji/ggu493

Sabaka, T. J., Tøffner-Clausen, L., Olsen, N., and Finlay, C. C. (2020). CM6: a comprehensive geomagnetic field model derived from both CHAMP and Swarm satellite observations. *Earth Planets Space*, *72*(1), 80. https://doi.org/10.1186/s40623-020-01210-5

Thébault, E., Vigneron, P., Langlais, B., and Hulot, G. (2016). A Swarm lithospheric magnetic field model to SH degree 80. *Earth Planets Space*, *68*(1), 126. https://doi.org/10.1186/s40623-016-0510-5

Walker, M. R., and Jackson, A. (2000). Robust modelling of the Earth's magnetic field. *Geophys. J. Int.*, *143*(3), 799–808. https://doi.org/10.1046/j.1365-246x.2000.00274.x

Winch, D. E., Ivers, D. J., Turner, J. P. R., and Stening, R. J. (2005). Geomagnetism and Schmidt quasi-normalization. *Geophys. J. Int.*, *160*(2), 487–504. https://doi.org/10.1111/j.1365-246x.2004.02472.x

Zhang, K. (2023). A novel geomagnetic satellite constellation: Science and applications. *Earth Planet. Phys.*, *7*(1), 4–21. https://doi.org/10.26464/epp2023019